

## Article

# Extended Stress–Strain Characterization of Automotive Steels at Dynamic Rates

Giuseppe Mirone <sup>1,\*</sup>, Raffaele Barbagallo <sup>1</sup>, Michele Maria Tedesco <sup>2</sup>, Daniele De Caro <sup>2</sup> and Matteo Ferrea <sup>2</sup>

<sup>1</sup> Department of Civil Engineering and Architecture, University of Catania, Via Santa Sofia 64, 95123 Catania, Italy; raffaele.barbagallo@unict.it

<sup>2</sup> C.R.F. S.C.p.A, Metals, Corso Settembrini 40, 10135 Turin, Italy; michele maria.tedesco@crf.it (M.M.T.); daniele.de-caro@stellantis.com (D.D.C.); matteo.ferrea@crf.it (M.F.)

\* Correspondence: gmirone@dii.unict.it

**Abstract:** Demanding structural applications require a detailed knowledge of the materials response up to the very late stages before failure. Ductile high-strength steels may undergo pronounced necking over the majority of their straining life; this makes a reliable stress–strain characterization difficult, especially at dynamic rates, because the self-heating from fast adiabatic dissipation may promote thermal effects interplaying with the strain rate effects. Further complications arise in deriving the postnecking flow curves when the material is a metal sheet due to geometrical issues intrinsic in the prismatic flat shape of the specimens. This paper focuses on the experimental derivation of the flow curves of DP1000 and MS1700 steels at strain rates ranging from 1 to 500/s. In addition, the moderately high temperatures achieved due to the self-heating at dynamic rates are imposed at static rates for separately investigating thermal and dynamic effects. Digital Image Correlation (DIC) and pixel counting optical techniques are used together with postprocessing procedures based on standard criteria and on physical considerations proposed by the authors. The resulting hardening curves are compared to each other and the advantages of the proposed method are discussed.



**Citation:** Mirone, G.; Barbagallo, R.; Tedesco, M.M.; De Caro, D.; Ferrea, M. Extended Stress–Strain Characterization of Automotive Steels at Dynamic Rates. *Metals* **2022**, *12*, 960. <https://doi.org/10.3390/met12060960>

Academic Editor: Seok Su Sohn

Received: 28 April 2022

Accepted: 26 May 2022

Published: 2 June 2022

**Publisher's Note:** MDPI stays neutral with regard to jurisdictional claims in published maps and institutional affiliations.



**Copyright:** © 2022 by the authors. Licensee MDPI, Basel, Switzerland. This article is an open access article distributed under the terms and conditions of the Creative Commons Attribution (CC BY) license (<https://creativecommons.org/licenses/by/4.0/>).

**Keywords:** sheet metal; strain rate; necking; flow stress; DIC

## 1. Introduction

The stress–strain characterization of sheet metals at high strains is crucial for many applications including, in particular, metal forming. Usually, the characterization relies on the classical tensile test on dog bone-shaped specimens. In an industrial context, very often, the characterization of materials is completed following the technical regulations. However, after the unavoidable onset of the diffuse necking, the extraction of the flow curve of the material is not straightforward. The basic extrapolation of the complete hardening curve using only tensile test data until the onset of necking is now widely viewed as insufficient. This issue is amplified by the modern advanced materials, exhibiting high values of ultimate tensile strength and ductility. Then, in order to exploit the full potential of advanced metals, the need for extended stress–strain characterization reliable up to fracture is clear. Therefore, several characterization procedures have been proposed with different approaches.

Many authors rely on the inverse approach [1,2] and Virtual Fields Method [3,4], i.e., the iterative update of the flow curve of the material until the difference between experimental results and the corresponding FEM simulations prediction is minimized under a certain threshold.

This approach is rather successful for the static characterization, although the flow curve can be affected by some preliminary modeling choices (associated or non-associated plasticity, yield function and plastic potential parameters), but it is prone to severe increase

in calculus complexity and to issues of non-unicity of the solution in case of dynamic strain-  
ing, where the flow stress expresses coupled dependencies on the strain, the temperature,  
and the strain rate.

On the other hand, direct procedures aim at the characterization of the constitutive  
curve of the material directly from the tensile experiments, without the need of iterative  
simulations. The classic approach, still widely used for its simplicity, relies on the engineer-  
ing values of stress and strain ( $\sigma_{\text{eng}} = F/A_0$ ,  $\epsilon_{\text{eng}} = \Delta L/L_0$ ) and transforms them into the  
corresponding true variables ( $\sigma_{\text{ture}} = \sigma_{\text{eng}}(1 + \epsilon_{\text{eng}})$ ,  $\epsilon_{\text{ture}} = \ln(1 + \epsilon_{\text{eng}})$ ). This transformation  
is based on the volume conservation of the gage length of the specimen and is rigorously  
correct only until the onset of necking. Afterwards, it loses accuracy and, in the case of very  
ductile materials, gives completely misleading information about the material behavior.  
Bridgman [5] pioneered the direct extrapolation of the flow curve of the material from  
tensile tests on cylindrical specimens using local measurements of the neck. Indeed, from  
the diameter of round specimens, it is possible to directly obtain the rigorous true stress  
 $\sigma_{\text{ture}} = F/A$  and true strain  $\epsilon_{\text{ture}} = \ln(A_0/A)$ . The true curve is coincident to the flow curve  
of the material until the onset of necking. Afterwards, the Bridgman method allows us to  
directly obtain the flow curve of the material from the true one. However, the Bridgman  
method is not easily applicable to rectangular specimens. Mirone proposed the MLR  
method [6], a corrective function which proved to be able to correct the true curve of the  
material into its flow curve with both cylindrical and rectangular specimens. However, in  
the case of rectangular specimens, in order to rigorously evaluate the cross-section area of  
the specimen, it is necessary to implement complex experimental setups such as 3D DIC.  
Peirs et al. [7] used DIC to correct the experimentally obtained engineering stress–strain  
curves from high strain rate SHTB tensile tests on Ti6Al4V specimens. They estimated the  
stress–strain curve beyond necking by considering the local logarithmic strain measured in  
the center of the specimen and deducing the true axial stress from the Hopkinson strain  
waves with the conversion from engineering into true stress values based on the locally  
measured strain. Abedini et al. [8] made a critical evaluation of constitutive character-  
ization techniques for sheet metals based on virtual tensile experiments. In particular,  
they compared the Area Reduction Method (ARM), based on the evaluation of the actual  
cross-section area of the specimen during the test in order to directly obtain the true stress  
 $\sigma_{\text{ture}} = F/A$  and true strain  $\epsilon_{\text{ture}} = \ln(A_0/A)$ , and the reduced size extensometer method  
(RSEM), which is in essence the above explained approach of Peirs et al. [7]. They concluded  
that the ARM method is insensitive to the specimen geometry, but it overestimates the flow  
curve of the material. It needs a correction such as the Bridgman [5] or the MLR [6] ones  
discussed above. On the other hand, Abedini et al. [8] concluded that the use of local DIC  
strains from a small surface extensometer within the necking region in the RSEM is not suit-  
able for the constitutive characterization of materials, leading to important overestimations  
of the flow curve. Mirone et al. [9] proposed a procedure able to transform the engineering  
curve easily obtainable from a tensile test with whatever cross-section geometry into the  
corresponding true curve.

The extrapolation of the material flow curve from static tensile tests is the base of the  
characterization of metals. However, further issues are present when the characterization  
and modeling regard different temperatures and strain rates. Indeed, despite the countless  
studies present in the literature, open issues still exist regarding the combined effects of  
strain, strain rate and temperature on the hardening behavior of materials. In particular,  
in the characterization procedure at high strain rates, it is fundamental to take into account  
a phenomenon that the authors and other researchers analyzed in great detail [10–18],  
i.e., the necking-induced spontaneous increase in the effective strain rate at the minimum  
cross-section of a specimen, despite the global elongation speed remaining nearly constant  
until failure. Indeed, the correlation between the effective local strain rate and the corre-  
sponding stress amplification is not straightforward, as also pointed out by Jacques and  
Rodríguez-Martínez [19]. Many authors tried to evaluate separate effects of temperature  
and strain rate. Chandran et al. [20] studied the DP1000 steel distinguishing the strain

rate and temperature effects by means of a correlation procedure. Hui and Rui [21] analyzed the DP1000 steel tensile behavior, finding that its yield and tensile strength increase monotonously with the strain rate while the uniform elongation and elongation at fracture firstly increase and then decrease with the strain rate. Cadoni et al. [22] analyzed the behavior of two advanced dual phase steels DP1200 and DP1400 at different strain rates and temperatures, finding that both materials are low strain rate sensitive. Liu et al. [23] analyzed the damage mechanism of DP1000 steel, finding that the fracture mode is dependent on the strain rate. Xia et al. [24] analyzed the Q&P processed Fe-0.25C-1.5Si-3.0Mn, finding that the material showed higher ultimate tensile strength and yield strength during high strain rate tensile deformation, while its total elongation showed an opposite trend. Ruggiero et al. [25] studied the behavior of ADI JS/1050-6 iron, finding that its ductility increases with temperature and strain rate. Scapin et al. [26] found that the copper thermal softening varies greatly with the strain rate. Kabirian et al. [27] found that hardening due to the twinning phenomenon in ECAPed AZ31 magnesium alloy, at the same strain rate, is more pronounced with lower testing temperatures. Jia et al. [28] studied the negative strain rate sensitivity and complex temperature sensitivity of 304 stainless steel at different strain rates and temperatures. Wen et al. [29] highlighted the influence of strain rate on the dynamic sensitivity and elongation at fracture of ultrahigh strength steels.

In this work, the tensile behavior at different strain rates and temperatures of two high-strength steels, identified as DP1000 and MS1700, will be analyzed in great detail. In particular, different direct characterization approaches will be used and compared in order to highlight the strengths and issues of each methodology.

## 2. Experimental Tests

Tensile tests were run on flat tensile specimens shaped as in Figure 1, which were made of DP700Y980T steel (briefly DP1000) and of CR1350Y1700T-MS steel (briefly MS1700).

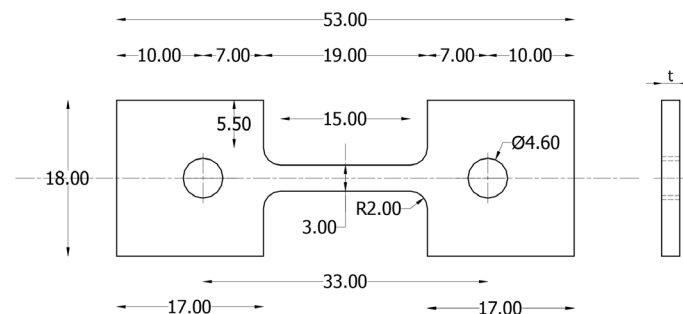


**Figure 1.** Tensile specimens (unit: mm).

The shape of the specimen was aimed at ensuring that a reasonable length undergoes a clean uniaxial stress state unaffected by shoulder effects (nominal length/width ratio = 5) and that the cross-section is as “thick” as possible for the given sheet thickness (nominal width/thickness ratio = 2) by reducing the specimen width and the overall specimen size. In fact, relatively high thickness helps a lot in contrasting the tendency to early localized necking of thinner specimens and then extending the specimen ductility. Tests previously performed by the authors on a Q&P automotive steel sheet of 2 mm thickness demonstrated that decreasing the specimen width from 12 to 5 mm increased the failure strain of 50% (from 0.35 to 0.55).

Tests at static and four dynamic rates were run at room temperature, while static tests were also run at temperatures of 100 and 200 °C. The complete series of tests conditions is reported in Table 1.

Static tests were run on a motor-driven testing machine equipped with climatic chamber (Figure 2c), slower dynamic tests at 1 and 10/s were run on a hydraulic testing machine capable of crosshead speeds up to 0.45 m/s (Figure 2a), and faster dynamic tests at 250 and 500/s were run on an 8 m direct-tension Hopkinson bar (Figure 2b).

**Table 1.** Experimental campaign.

Test Name	Strain Rate [1/s]	Temperature [°C]
materialname-S	$3 \times 10^{-4}$	20
materialname-D01	1	20
materialname-D10	10	20
materialname-D250	250	20
materialname-D500	500	20
materialname-S-T100	$3 \times 10^{-4}$	100
materialname-S-T200	$3 \times 10^{-4}$	200

**Figure 2.** Testing equipment for experiments: (a) Hydraulic machine for slower dynamic tests, (b) SHTB for faster dynamic tests, and (c) motor-driven machine with climatic chamber for static tests at different temperatures.

The tests were run at constant elongation speed, which delivers constant strain rate only up to the necking onset; in the next sections, the quantitative assessment is discussed of the effective strain rate after necking onset deviating from the nominal strain rate of the test.

Optical measurements were taken for local strains (DIC) and for displacements of relevant points on the surface of the specimens (pixel count), on images acquired by a speed camera at frame rates up to 200,000 fps for the faster dynamic tests.

The minimum image resolution at the highest adopted frame rate was set in order to guarantee that the specimen dimension (3 mm width) was always acquired with at least 70 pixels, ensuring an adequate accuracy in both strain and displacement measurements. Frames extracted from the video acquisitions are reported in the next sections.

Current tensile force, specimen elongation and specimen width contraction were recorded at appropriate time intervals together with full-field strain maps from DIC post-processing, for guaranteeing that at least 25 points of a true curve were calculated for the faster tests at 500/s; much more points were available for slower tests.

Figure 3a,b show the histories of load signals from two Hopkinson bar tests at  $500 \text{ s}^{-1}$ , according to the one-wave, two-wave and three-wave procedures. Considering that the initial rise time and the elastic loading cover nearly  $70 \mu\text{s}$ , the first and the second plots are, respectively, representative of the plastic loading under the best and the worst equilibrium conditions achieved in the present experimental campaign. As clearly visible, the three-waves procedure is less sensitive to equilibrium issues than the two other load estimates; therefore, the former is adopted in the next sections for the calculation of the load.

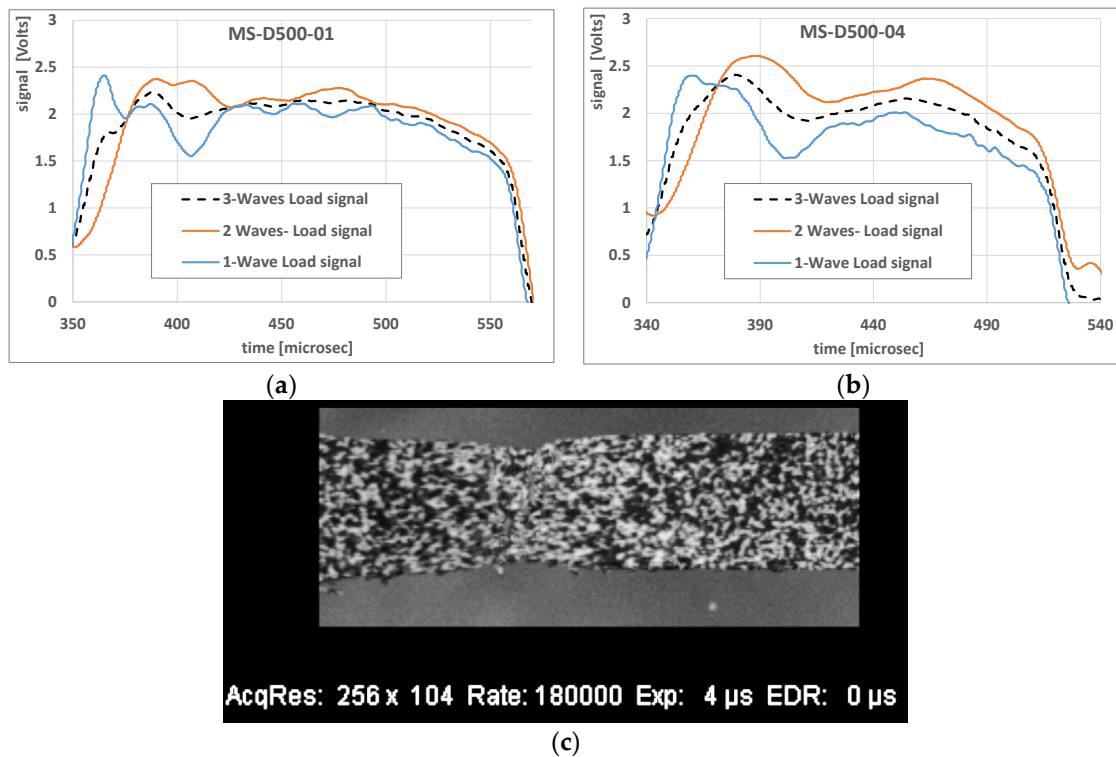


**Figure 3.** Load histories according to the one-wave, two-wave and three-wave procedures of MS1700-D500-01 (a) and 04 (b) dynamic SHTB tests. Typical frame at incipient failure from a dynamic test (c).

Figure 3c reports the adopted frame rate of 180 kfps which, assuming a duration of 130  $\mu\text{s}$  of the plastic straining, delivers 24 frames suitable for plastic strain and displacements measurements all over the tests at hand.

The processing of experimental data for the derivation of the true curves is made according to different procedures, as detailed in the next section.

### 3. Procedures for Determining the True Stress–True Strain Curves

True stress and true strain are defined as the stress and the finite strain acting along the axial direction of a tensile specimen, averaged over the current minimum cross-section.

Within the necking onset of smooth specimens, the above variables are identical to their “equivalent” counterparts:

$$\varepsilon_{\text{Eq}} = \varepsilon_{\text{Ture}}, \sigma_{\text{Eq}} = \sigma_{\text{Ture}} \quad (1)$$

The necking onset introduces progressively increasing stresses parallel to the thickness and to the width of smooth flat specimens (which means progressively increasing stress triaxiality over the neck section), together with spatial gradients of the stress and strain distributions.

The effect of stress triaxiality consists of the Mises flow stress progressively deviating from the true stress. Such an issue can be solved by different postnecking corrective functions [5,6], which are capable of transforming the current values of  $\sigma_{\text{Ture}}$  from experiments into current estimates of  $\sigma_{\text{Eq}}$ .

Instead, the effect of stress–strain gradients within the necked specimen spoils the experimental derivation of  $\sigma_{\text{Ture}}$  to different extents, depending on the adopted experimental procedure.

Referring to a smooth flat specimen as in Figure 4, various procedures can be adopted for calculating  $\varepsilon_{\text{Ture}}$  and  $\sigma_{\text{Ture}}$ , delivering different formulations of the true stress–true strain data (briefly of the true curves), according to Equations (2)–(7).

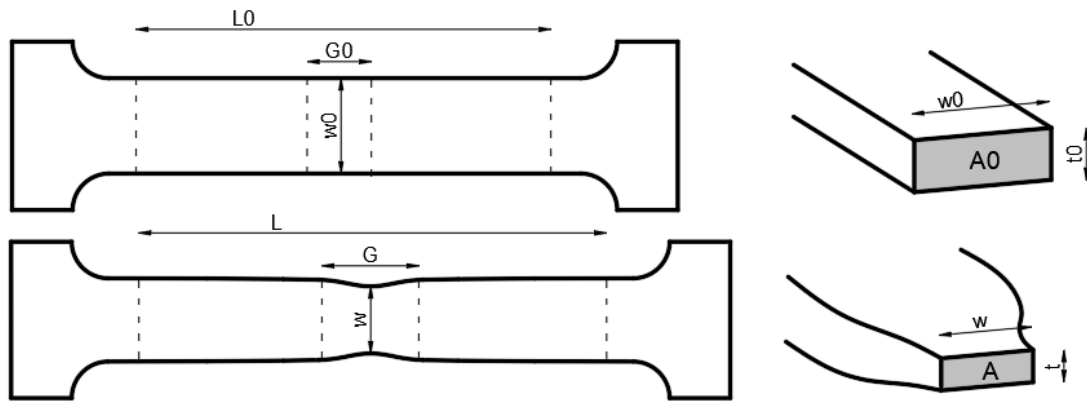


**Figure 4.** Possible geometrical parameters for true stress–true strain evaluations.

### 3.1. Length-Based with Standard Gage Length

This is the most widely used approach, as it simply requires recording the elongation of a rather long gage length  $L_0$ , which is usually close to 3–5 times the specimen width according to the most known technical standards.

$$\varepsilon_L = Ln\left(\frac{L}{L_0}\right), \sigma_L = \frac{F}{A_0} \cdot \frac{L}{L_0} = \frac{F}{A_0} \cdot e^{\varepsilon_L} \quad (2)$$

The true curve obtained in this way reflects the material behavior averaged over the entire specimen volume, as it assumes that  $A_0 \cdot L_0 = A \cdot L$ , which is only valid before necking; therefore, Equation (3) largely misses the necking effect, which only regards a small fraction of the specimen volume.

The validity of this formulation is limited to the onset of the necking and tensile instability.

### 3.2. Length Based with Arbitrary Short Gage Length

As shorter gage lengths are adopted, always centered on the neck section, the resulting true curves will reflect the material behavior averaged over a smaller specimen volume including the most-strained neck section together with less strained neighboring cross-sections, as the volume conservation is based on  $A_0 \cdot G_0 = A \cdot G$ , which is less inaccurate than before. Now, the true curve reflects a “less global”/“more local” material behavior than before, but the effective material response at the neck section is not yet really unveiled.

$$\varepsilon_G = Ln\left(\frac{G}{G_0}\right), \sigma_L = \frac{F}{A_0} \cdot \frac{G}{G_0} = \frac{F}{A_0} \cdot e^{\varepsilon_G} \quad (3)$$

This approach is accurate only within the onset of diffused necking and tensile instability, although the error it develops after necking decreases as the adopted gage length  $G_0$  decreases.

### 3.3. Area-Based

This approach corresponds to using a zero-extension gage length; therefore, it delivers the material behavior averaged onto the two-dimensional current neck section instead of being averaged onto a partial or total specimen volume as in the two former cases.

$$\varepsilon_A = Ln\left(\frac{A_0}{A}\right), \sigma_L = \frac{F}{A} \quad (4)$$

This approach seems slightly more complicated than the former ones because the current minimum cross-section  $A$  should now be acquired from experiments instead of the current gage lengths  $G$  or  $L$  of the former cases.

The following considerations show that such difficulties are only apparent and are largely balanced by great improvements in the accuracy of the resulting true curve.

After the first diffused necking, which is associated to the tensile instability, flat specimens can undergo a secondary localized necking which distorts the rectangular shape of the neck section by curving and depressing its edges, as qualitatively depicted in Figure 5. The envelope of the depressions on the cross-sections of the edges generates the typical thinning band inclined at nearly 55 degrees, which is more evident in case of thinner specimens.

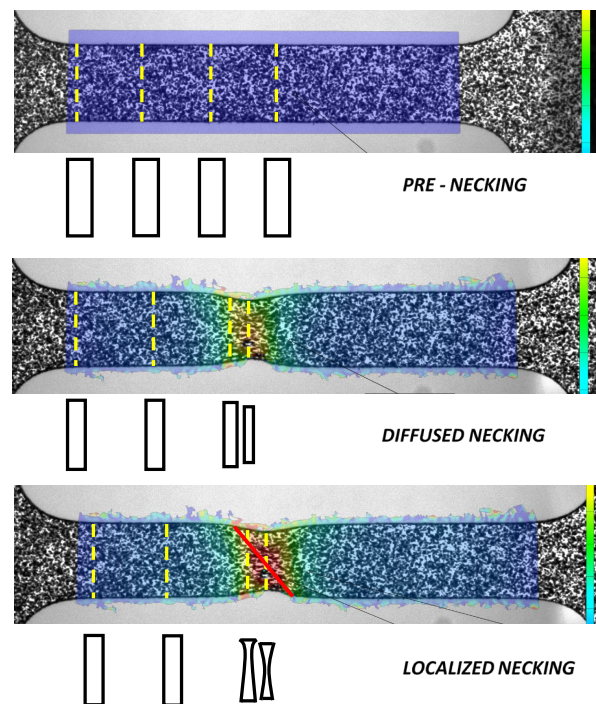


**Figure 5.** Cross-sections of a flat tensile specimen before necking, after diffused necking, and after localized necking.

For isotropic materials, the thinning of the cross-sections of tensile specimens evolves in a proportional fashion so that the constancy of the width to thickness ratio  $w/t$  is preserved all over the test; this allows us to determine the current neck section from a simple measurement of the current width according to Equation (5).

$$\frac{w}{t} = \frac{w_0}{t_0} \rightarrow t = w \cdot \frac{t_0}{w_0} \rightarrow A = w \cdot t = w^2 \cdot \frac{t_0}{w_0} \quad (5)$$

The width and thickness of the failed specimens of the DP1000 and MS1700 steels investigated in this work, optically measured as in Figure 6, confirm that a remarkable constancy of the ratio  $w/t$  is preserved until failure, despite the localized necking possibly causing a progressive distortion of the edges of the cross-section on the necked zone, as also visible in the same figure.

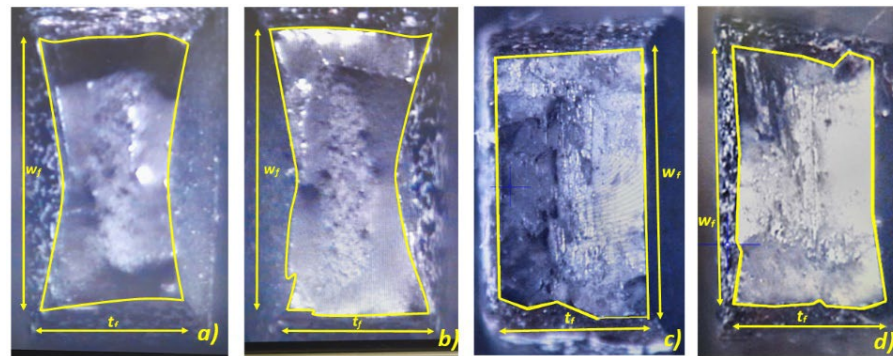


**Figure 6.** Failed neck sections of DP 1000 (a,b) and MS 1700 steels (c,d) from static tests (a,c) and dynamic tests at  $500 \text{ s}^{-1}$  (b,d).

The distortion of the neck section is more pronounced for the DP1000 steel, while it is almost negligible for the MS1700 steel, which is quite expectable as the former steel is more ductile and undergoes a more pronounced localized necking than the latter steel.

The ratio  $\frac{w}{t}$  of the four representative specimens considered in Figure 6 evolves according to Table 2 from test beginning until failure. The constancy of  $\frac{w}{t}$  implies that the area derived as in Equation (5) is accurate until the localized necking develops, while it afterwards progressively overestimates the effective neck section by continuing to assume a shape of the neck section with straight edges instead of the sunken shape especially visible in the DP1000 fractured neck.

**Table 2.** Variability of the width/thickness ratio for static and dynamic tests of DP1000 and MS1700 steels.

	$\frac{w}{t}$ Undeform	$\frac{w}{t}$ @ Failure
DP1000-S	1.91	1.96
DP1000-D500	1.91	2.06
MS1700-S	1.83	1.80
MS1700-D500	1.80	1.71

This, in turn, means that Equation (4) is accurate before the localized necking takes place, but afterward, it progressively underestimates both the true stress and true strain.

The magnitude of the maximum approximation of Equation (5) at failure is evaluated by assessing the effective resisting area as the difference between the gross rectangular area  $w \cdot t$  and the dashed area as in Figure 7. After the images of the broken specimen are imported in a CAD environment and are properly scaled, polygons are drawn for approximating the fracture surfaces, and the corresponding areas are then delivered by simple pixels-counting functions.

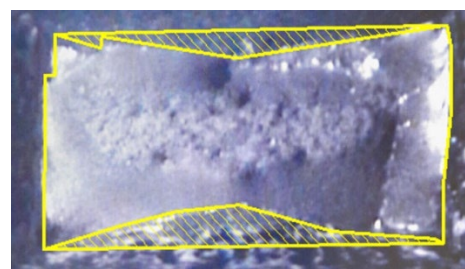


**Figure 7.** Assessment of the effective resisting area at failure for the DP1000-S test.

The ratio of apparent area/effective area, both measured on the fractured specimens, is assumed to also apply to the last unbroken cross-section before failure, whose area was already determined by Equation (5).

The ratio of the effective neck sections to the apparent neck sections at failure is reported in Table 3 for the test series of static and D500 dynamic tests of DP1000 and MS1700 steels, together with the logarithmic strains at failure from Equation (4), which were calculated with both the apparent area and the corrected area.

**Table 3.** Apparent and effective cross-sections at failure for DP1000 and MS1700 steels (series-averaged data).

	Ratio $A_{eff.}/A$	Area-Based Failure Strain	Corrected-Area Failure Strain
DP1000-S	0.81	0.51	0.73
DP1000-D500	0.82	0.48	0.68
MS1700-S	0.90	0.36	0.46
MS1700-D500	0.90	0.33	0.44

As already suggested by Figure 6, the MS1700 steel is confirmed to exhibit a much lower distortion of the rectangular cross-section than the DP1000 one.

The effective corrected neck sections at failure from all tests can be then introduced in Equation (4), delivering a “corrected-area” failure point for each true curve.

### 3.4. Local Strain-Based (DIC Peak with Few-Pixels-Sized Gage Length)

This procedure tries to exploit the availability of local strain values varying along the width of the neck section for estimating a local axial stress, which is variable too along the transverse axis of the neck section.

Local strains are typically available by optical methods such as DIC or elongation measurement by pixel count with very small gage lengths across the neck at different transverse locations.

We can discretize the flat specimen according to general n-segments subdivisions along its width as in Figure 8, so that each initial sub-area  $a_0$  of the cross-section  $A_0$  is finite but small enough (comparable to the multiple-pixel-sized facet of DIC strains) that single local DIC strain readings can be assumed to apply over each single sub-area.

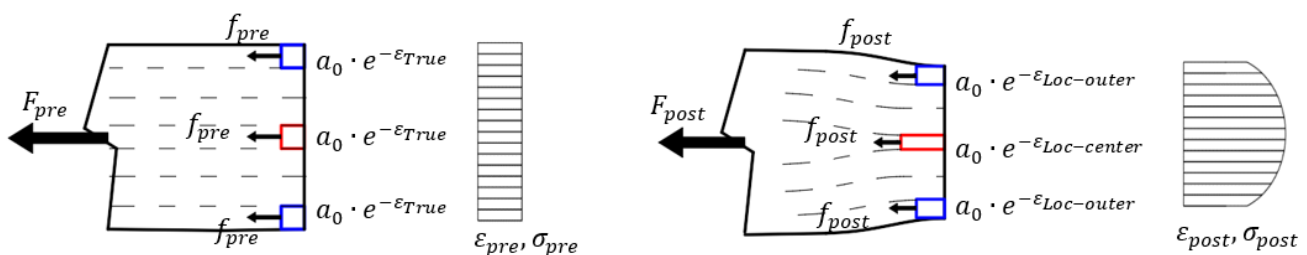


**Figure 8.** Discretized specimen for deriving the local-strains-based true curve.

In the undeformed configuration, each sub-area  $a_0$  is the  $n$ -th fraction of the total cross-section area  $A_0$ :  $a_0 = A_0/n$ .

During plastic straining, each sub-area undergoes its own local plastic strain  $\epsilon$ , which makes it shrink according to Equation (6):

$$a_0 \cdot e^{-\epsilon} \tag{6}$$

Therefore, the knowledge of local strains delivers the current size of each shrunken sub-area at each stage of a tensile test. Before necking onset, the plastic strains of all sub-areas are equal to each other and to  $\epsilon_{True}$ , while after necking onset,  $\epsilon$  varies along

the width, with a peak at the center ( $\varepsilon_{Loc-center}$ ) and lower values at the outer neck points ( $\varepsilon_{Loc-outer}$ ). Then, after necking onset, the sub-area at the neck center becomes smaller than the sub-areas at the outer sides of the neck section, as illustrated in Figure 8.

If the elementary loads acting on each sub area are known, then the local axial stresses can be simply obtained as the values of the elementary load/sub-area ratio.

Before necking onset, the unit axial forces are certainly equal to each other,  $f_{pre} = F_{pre}/n$ , which delivers the trivial uniformity of the axial stress as  $\sigma_{z-pre} = f_{pre}/(a_0 \cdot e^{-\varepsilon_{true}}) = F_{pre}/A_0 \cdot e^{\varepsilon_{true}}$ .

After necking onset, it is assumed that  $f_{post} = F_{post}/n$  continues to apply, which constitutes the main approximation of this procedure also common to the classical transformation of engineering curves into true curves according to Equations (2) and (3). In fact, such an assumption also corresponds to the assumption that the engineering stress–strain curves calculated either over the entire cross-section  $A_0$  or over finite subsections  $a_0$  are identical to each other.

Then, the ratio of each elementary force to each elementary shrunk area delivers the distribution of  $\sigma_{z-post}$  in Equation (7), where the variability of  $\varepsilon_{Loc}$  along the transverse direction with a peak at the neck center induces a similar spatial variability to the axial true stress.

$$\sigma_{z-post} = f_{post}/(a_0 \cdot e^{-\varepsilon_{Loc}}) = F_{post}/A_0 \cdot e^{\varepsilon_{Loc}} \quad (7)$$

The assumption  $f_{post} = F_{post}/n$  corresponds to assume that the variability of  $\sigma_{z-post}$  along the width of the neck section is only driven by the variability of  $\varepsilon$  along such direction, neglecting the gradients of the elementary forces  $f_{post}$  likely induced by the postnecking hydrostatic stress components (independent of plastic strain). This is expected to cause an overestimation of  $\sigma_{z-post}$  at the outer points of the neck width and underestimation at the midpoint of the neck width.

In order to extend as much as possible the plastic range of the true curve obtainable by Equation (7), the relevant history of  $\varepsilon_{Loc}$  can be acquired at the most strained location over the specimen surface, which is the midpoint of the width of the necked specimen.

### 3.5. Details about the Area-Based and the DIC Peak-Based Procedures

The area-based true curves, the corrected-failure true curve endpoints and the DIC peak-based true curves reflect the same local approach with respect to the stress–strain gradients along the specimen axis, but they still incorporate some mutual differences from the viewpoint of the stress–strain variability within the specimen cross-section, according to the scheme of Figure 9.

The area-based approach delivers the current neck-averaged axial stress assuming a “gross” apparent neck section detectable by just the current minimum width  $w$  according to Equation (5). If the neck section of the specimen remains quite rectangular until failure (materials with moderate ductility), then such a method can be accurate; if instead, the cross-section distorts considerably before failure (more ductile materials), then this approach underestimates the late stages of a true curve because it neglects both the loss of resisting area due to the sinking edges of the neck section and the remarkable non-uniformity of stress over such a cross-section.

The corrected area-based approach delivers a more accurate average of the current axial stress at failure, since the effective neck area is considered, instead of the apparent one, for bearing the current load. In addition, the logarithmic ratio between initial and failure neck section now expresses the effective average of the axial strain over the neck section, so that the coupling of the failure stress and strain according to this procedure is not affected by conceptual approximations.

The DIC peak approach uses the current maximum local strain on the specimen surface for transforming a global average engineering stress,  $F_{post}/A_0$ , into an estimate of the local according to Equation (7).

If the specimen is thin enough, then no strain gradients occur along the thickness, so that the strain distribution acquired on the specimen surface by the DIC technique is also

representative of the inner layers of the neck section: in this case, the DIC strain distribution is perfectly representative of the entire neck section, and its peak is obviously higher than the section-averaged strain, as depicted in Figure 9c.

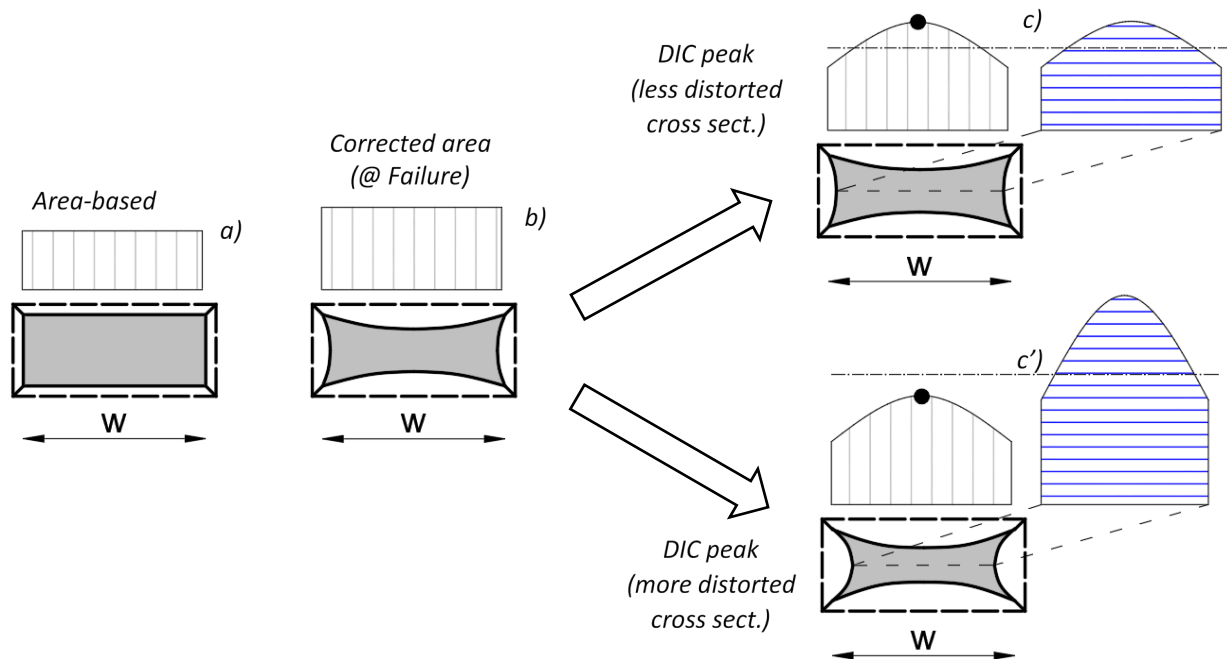


**Figure 9.** Different possible evaluations of the postnecking strain: (a) Area-based, (b) corrected area at failure, and DIC peak in the case of less distorted cross-section (c) and more distorted cross-section (c').

If instead the specimen is thick and its cross-section is greatly distorted, then the strain gradients along the thickness can be remarkable, and the DIC strains on the surface may also be lower than those on the specimen midplane: in this case, the peak of the DIC strain distribution may be either greater or lower than the neck-averaged strain, depending on the intensity of the strain gradients across the thickness.

Summarizing, the area-based procedure is accurate past the onset of the diffused necking, but as also the localized necking takes place, then such a curve progressively underestimates the section-averaged true curve.

The corrected area-based procedure delivers an estimate of the endpoint of the section-averaged true curve, where the possible approximations only lie in the assessment of the distortion degree of the area at fracture.

The intrinsic approximation of the DIC peak-based approach lies in relating macroscopic forces over the neck section to locally estimated peak strains; therefore, the resulting estimate of the stress–strain curve should be higher and longer than the neck-averaged true curve (the case of Figure 9c), although it might also be lower and shorter under special circumstances (the case of Figure 9c').

#### 4. Comparison and Selection of Procedures

Before implementing the above procedures to the entire set of experimental data, a preliminary screening is made by comparing the four series of true curves for the static tests DP1000-S20 and MS1700-S20, which are representative of the greater ductilities and greater distortion levels of the cross-sections for each material. The most performing procedures will be then selected for being applied to the results of the complete experimental campaign in order to assess the response of the two materials to high strain rate and temperature.

Figure 10 shows the experimental results of two static tests for each metal, evidencing that after necking onset, the elongation-based strain histories greatly depend on the arbitrary choice of the initial gage length and barely reflect the localizing deformation, leading

to huge underestimations of the strain and the stress all over the postnecking phase, which for these metals covers the greater part of the whole plasticity range.

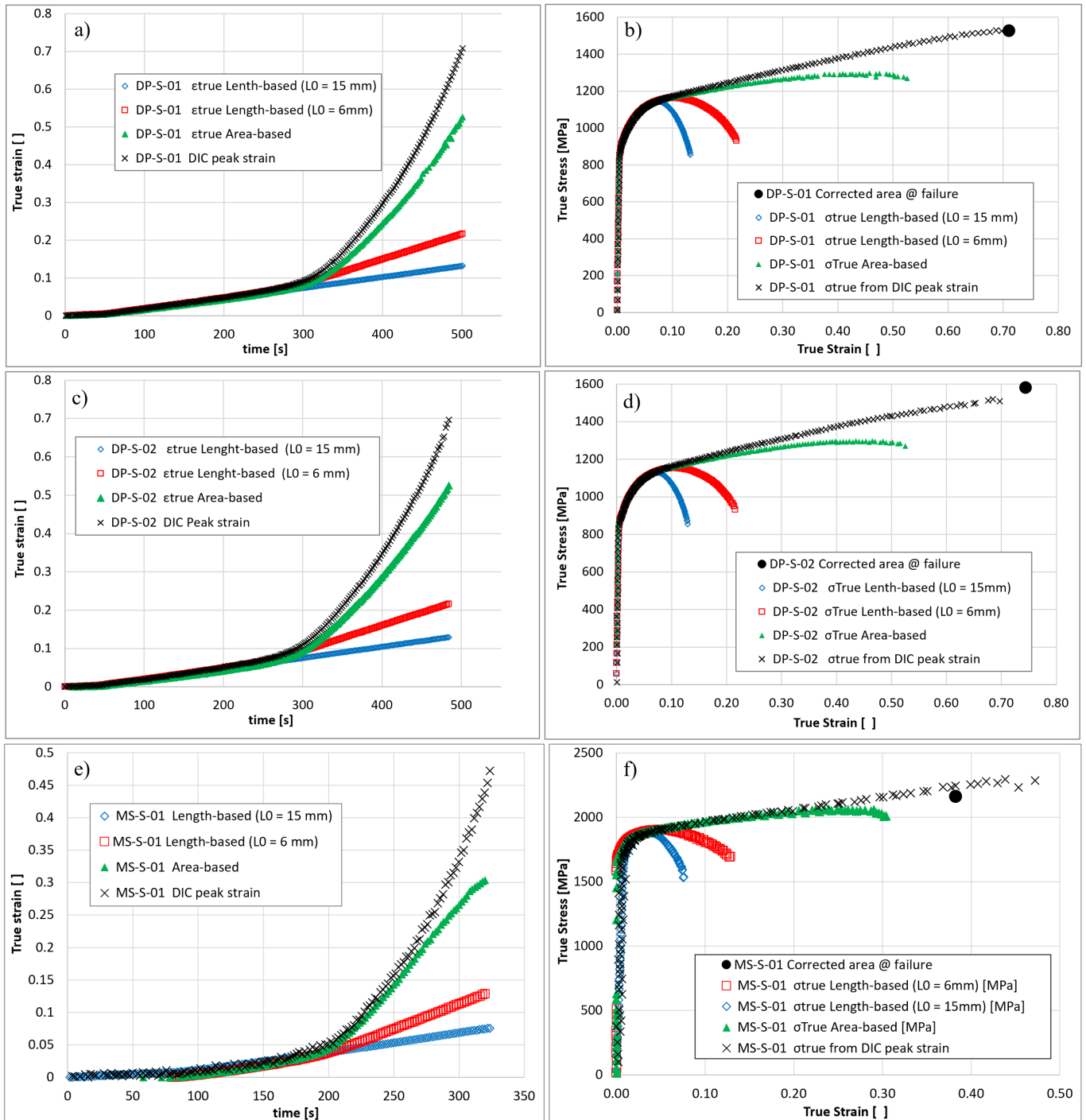
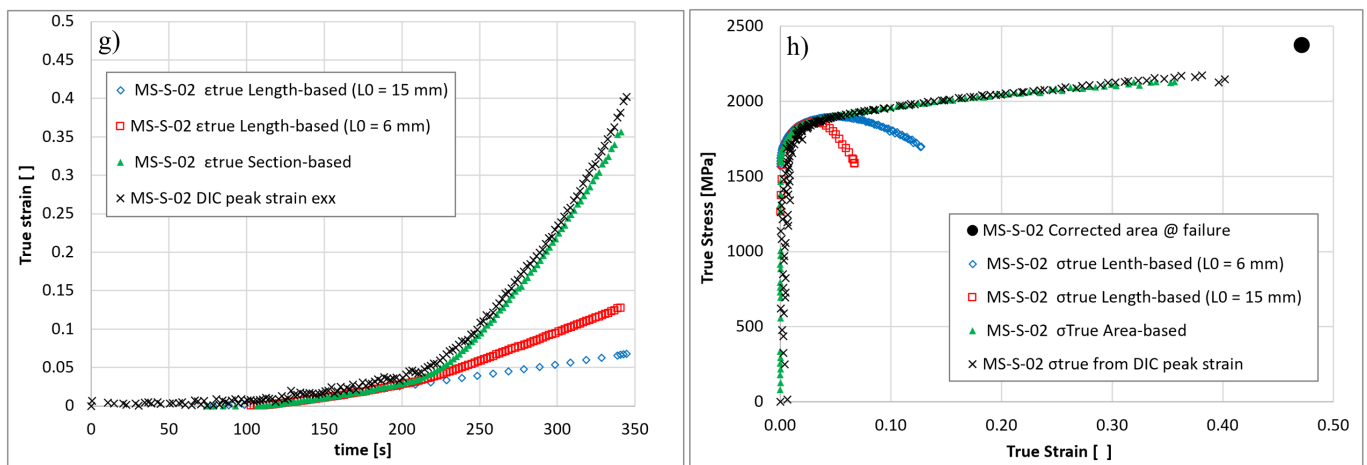


Figure 10. Cont.



**Figure 10.** Evaluation of strain histories and true stress-strain curves according to the four procedures (length-based with two different gage lengths, area-based, DIC peak strain, and corrected area at failure) for two static tests of each metal, i.e., DP-S-01 (a,b), DP-D-02 (c,d), MS-S-01 (e,f), MS-S-02 (g,h).

The area-based strain measurements and the local DIC peak measurements over the neck section deliver much more accurate predictions than the length-based ones, extending far beyond the onset of the diffused necking and up to strains  $\varepsilon \approx 0.2$ ; then, a difference progressively builds up between the area-based and the DIC peak curves.

This difference can be attributed on one side to the area-based approach underestimating stresses and strains because Equation (5) loses accuracy as the cross-section starts distorting, and on the other side to the DIC peak measurements, which are frequently affected by the choice of the measurement point on the specimen surface and by highly local noise and correlation issues at large strains.

In fact, at the high strains achieved by the metals at hand, the DIC technique at the local scale can be rather sensitive to the optical quality of the speckle pattern and to the choice of the analysis parameters. Fortunately, decorrelation or poorly accurate outcomes are limited to the final stages of the tests and to localized spots, which are easily detectable as sharp discontinuities in the spatial distribution and/or the temporal evolution of displacements and strains.

All the stress–strain curves in Figure 10 are quite repeatable for both the DP1000 and the MS1700 steels, although the DIC peak curves are slightly more scattered than those from the area-based and from the length-based procedures.

In addition, the failure strains are quite repeatable for the DP1000 steel, while those of the MS1700 are rather scattered.

The area-based strains at failure are always smaller than those from the corrected-area procedure, which is quite obvious; the DIC peak readings at failure are expected to go beyond the corrected-area predictions (peak strains on the surface greater than the neck-averaged values according to Figure 9c); instead, they are found to be quite scattered above and below the corrected-area ones, which reflects the noisy response of late DIC readings at the local scale.

The evidence in Figure 10 confirms the remarkable linearity of the postnecking true curve up to failure and suggests that a reasonable estimate of the plastic response of a material can be obtained by connecting the pre-necking true curve to the corrected-area failure point through a simple straight line.

Such an estimate greatly extends the range of validity of the length-based true curves (of a factor 10 to 15 for the metals at hand) and can be considered rather general, as it is not affected neither by the underestimated cross-section of the area-based procedure at late strains nor by the compatibility of local strains to global loads intrinsic in the DIC–peak procedure.

For the dynamic tests, also, the strain rate can be derived according to the different viewpoints discussed above: the trends of the length-based and area-based strains, measured at known time intervals, are approximated by best fit functions of the time which are successively derived, leading to the strain rate vs. time curves.

In Figure 11a, the length-based, area-based and DIC–peak strain histories are reported for the DP-D250-01 test together with the approximating best fit curves, while Figure 11b reports the corresponding strain rate vs. strain evolutions, which are briefly addressed ahead as strain rate histories.

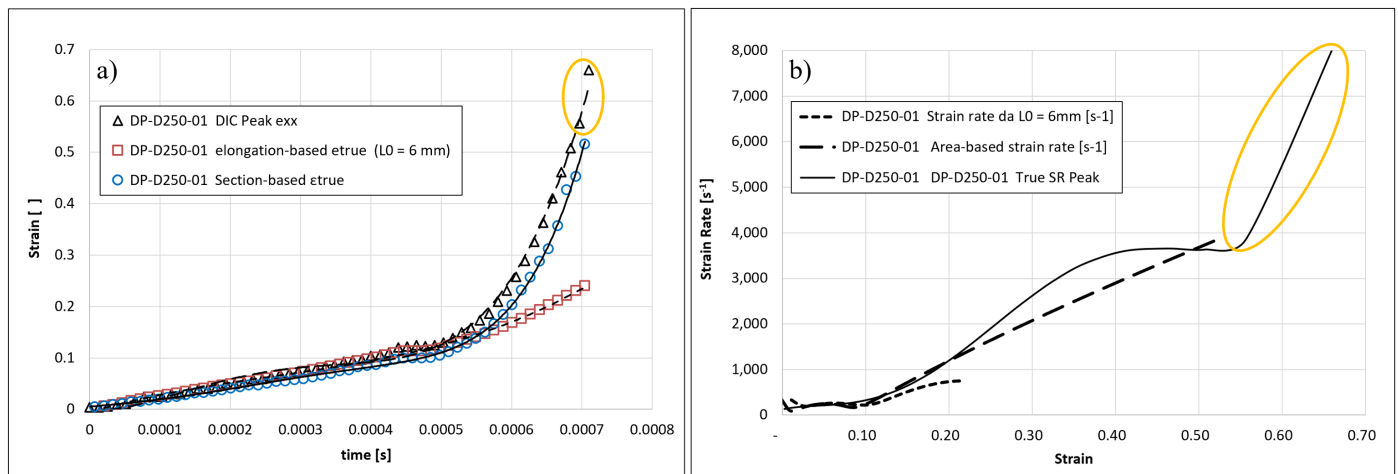


**Figure 11.** Dynamic SHTB DP-D250-01 test: Strain vs. time trends (a) and resulting strain rate histories (b).

The main message conveyed by such figure is that, as already demonstrated by the authors and by other researchers in [10–18], the imposed strain rate only remains constant (plateau at  $\dot{\epsilon} \approx 250$  /s) until the necking onset; then, it rapidly increases within failure, up to ten times the plateau.

The area-based strains and the local DIC strains allow to detect such a steep surge of strain rate occurring after necking onset because of the progressing strain localization, while the length-based strains cannot obviously reflect such phenomena.

Figure 11 also confirms that the DIC peak readings at incipient failure are more prone to interpretation issues than those at earlier test stages: in fact, the single last measurement of DIC peak strain ( $\epsilon$  passing from  $\epsilon \approx 0.55$  to  $0.65$ ) forces the strain rate history to an abrupt jump ( $\dot{\epsilon}$  passing from  $4000$  to  $8000$   $s^{-1}$ ), which likely does not express any real material response but just constitutes an artefact due to the unsteady nature of DIC readings for such highly local strain gradients.

The considerations made above about length-based, area-based, corrected-area and DIC peak procedures are especially relevant for materials such as those at hand, whose postnecking range covers a large fraction of the whole straining life.

In fact, the necking onset for tests DP-S and MS-S, respectively, occurs at strains around 0.07 and 0.03, while the failure strains are greater than 0.54 and 0.36: therefore, the above necking-related issues affect around 90% of the straining life of both metals.

It is also worth noting that the reverse-engineering approach to the stress–strain characterization based on finite elements iterative runs, while useful at static rates where the only relevant variable is the strain, is less exploitable at high rates where also strain rate and temperature drive the material response and, apart from the increase in the complexity of the reverse problem, can also induce non-unicity solution problems.

This makes it clear why a reliable procedure for the direct stress–strain characterization of ductile metals undergoing thermal or dynamic effects is highly desirable.

According to the outcomes of this section, the data from all experiments are processed in the next sections according to the area-based, the corrected-area-based and the DIC

peak-based approaches alone, for assessing the mechanical response of the DP1000 and MS1700 steels with the awareness of the possible approximations intrinsic in the procedures for the extended material characterization at large postnecking strains.

## 5. Experimental Results

For each experimental condition (same material, strain rate and temperature), three tests are run for statistical and error-mitigation purposes. Figure 12 shows the experimental repeatability for the entire test series of static loading (lowest scattering), intermediate dynamics by hydraulic testing machine (intermediate scattering) and high rate dynamics by Hopkinson bar (higher scattering of the experimental campaign).

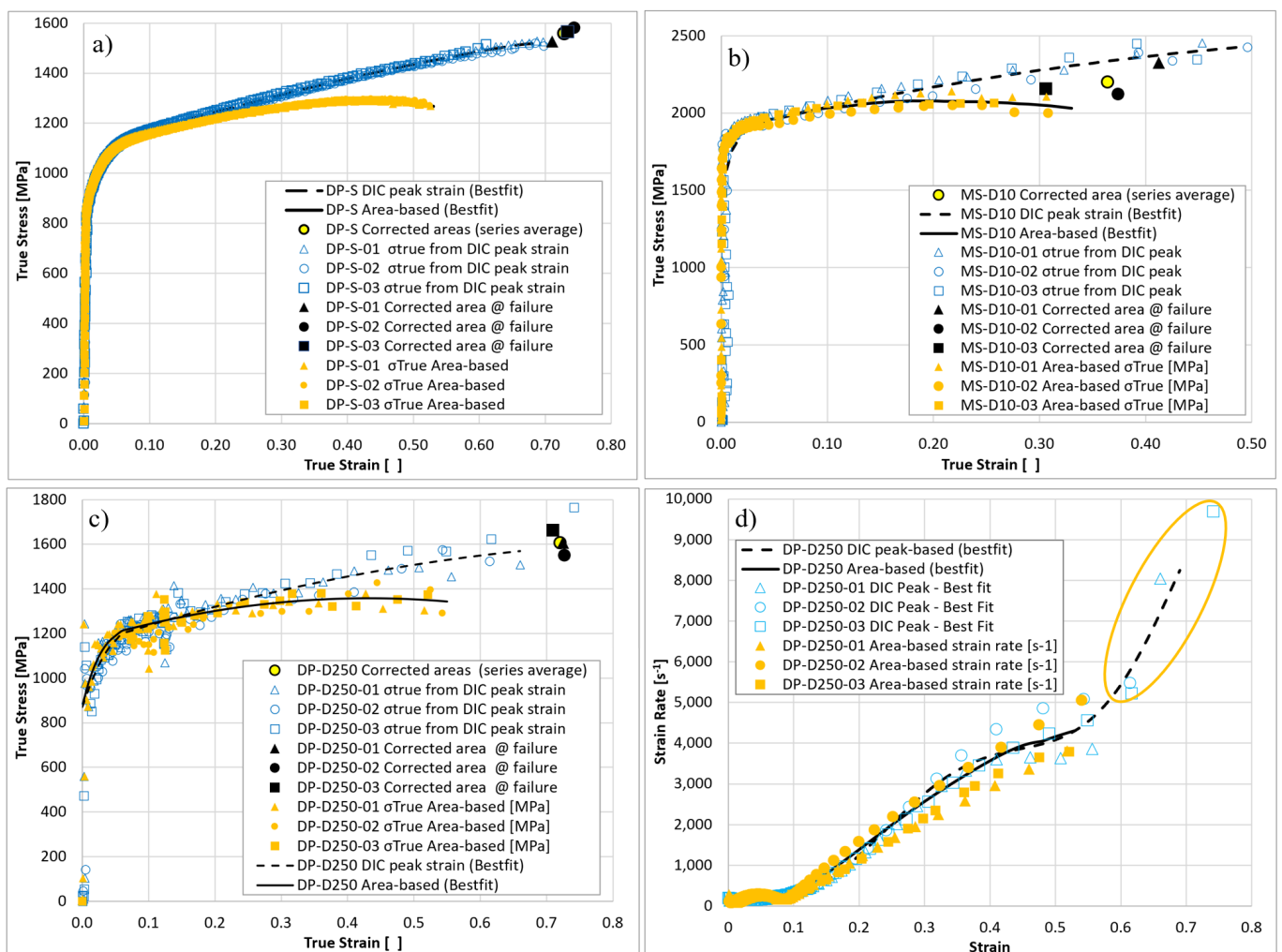


**Figure 12.** Repeatability of the experiments: DP static true stress-strain curves (a); MS dynamic true stress-strain curves at 10 s<sup>-1</sup> (b); DP dynamic experiments at 250 s<sup>-1</sup> true stress-strain curves (c) and strain rate histories (d).

The series-averaged true curves and strain rate histories in Figure 12 are adequately representative of the corresponding experimental series for both area-based and DIC peak procedures, although the latter approach generates a fictitious drift of the strain rate at very late test stages (see encircled data in the strain rate plot), as already seen in Figure 11. This final feature of the strain rate history can either express correlation issues of the last DIC frames or local failure initiation at inner material points within the specimen not yet detectable by the overall view of the specimen surface.

For the DP1000 steel, the corrected-area failure point is nicely aligned with the true curve from the DIC peak; instead, for the MS1700 steel, the corrected-area failure strain is rather intermediate between the final strain of the DIC peak true curve and that of the area-based true curve.

The series-averaged static response of the DP1000 steel is also compared in Figure 13 to three stress–strain curves from the literature for the same class of steel (Chandran et al. [20], Hui and Rui [21] and Alharbi et al. [30]).

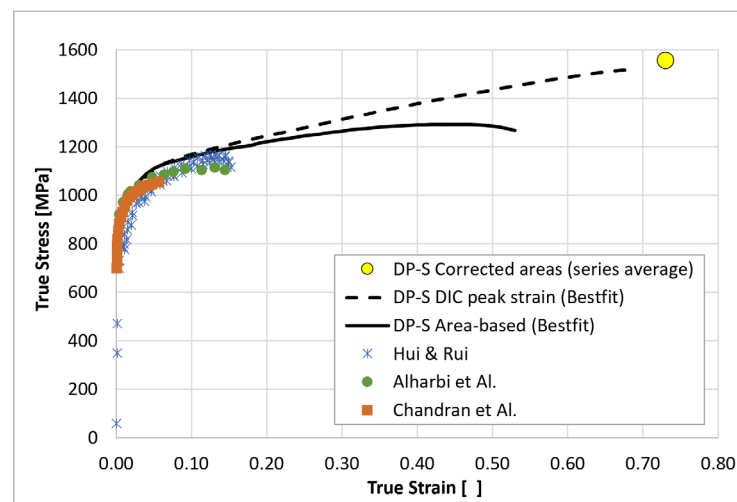


**Figure 13.** Comparison with true curves from the literature—steels of the class DP1000 according to different procedures.

All the curves in Figure 13 are closely packed together up to remarkable strain levels around 0.15. The postnecking range is not even present in the true curves from the literature, as it is acknowledged that in such a strain range, the length-based procedures do not deliver useful information about the material plasticity.

The behavior of the two steels is analyzed below by comparing the series-averaged stress–strain curves and strain rate histories under the various testing conditions considered.

### 5.1. Static Tests at Room and High Temperature

The static tests at high temperature were run in a climatic chamber of sufficient size for ensuring temperature uniformity. Furthermore, a stabilizing time was taken after the specimen was installed in the chamber, before the effective test start, for also preventing the thermal dilatation to generate stresses superimposed to the tensile ones.

The true curves from static tests at different temperatures are compared to each other in Figure 14 for both steels.

The static plasticity of the DP1000 steel exhibits a negligible sensitivity to the temperature as the true curves at different temperatures are almost coincident to each other, except for their endpoints, which retreat at 100 and 200 °C, indicating a temperature-driven decreasing ductility.

On the contrary, the steel MS1700 exhibits a clearly visible thermal-hardening opposite to the more usual thermal softening, as the true curves at higher temperatures are higher than the true curve at room temperature. A more typical thermal softening is barely detectable at very early plastic stages (strains below 5%, that is before necking onset).

Assuming a general multiplicative interaction of plastic strain and temperature on the flow stress, the thermal effect is quantified here by the ratio between the flow curve at given temperature to the flow curve at room temperature.

$$S(\varepsilon, T) = \frac{\sigma_{Eq}(\varepsilon, T)}{\sigma_{Eq}(\varepsilon, 20)} \quad (8)$$

It is worth noting that the true stress only equals the flow stress before necking onset. Both the steels at hand exhibit a very early necking onset and a rather remarkable ductility; therefore, a postnecking correction is essential for transforming the true stress into a reasonable estimate of the flow stress (e.g., Bridgman correction [5]).

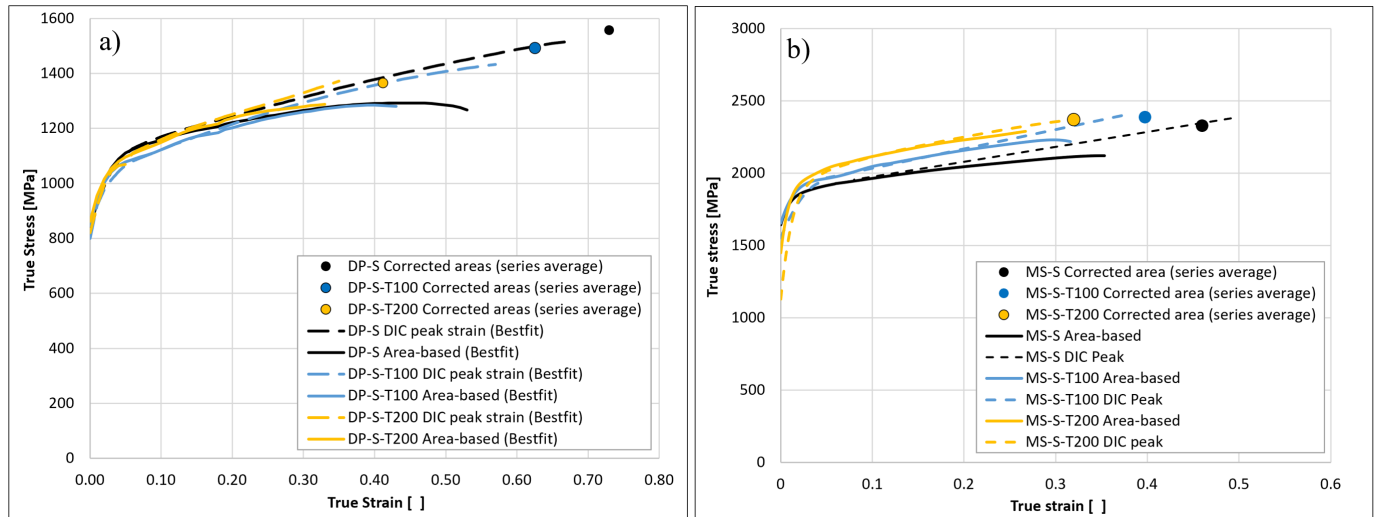


Figure 14. Thermal effect at static rates for the DP (a) and MS (b) materials.

Here, the correction by Mirone et al. [6] is adopted, consisting of the MLR function of the postnecking strain, which is material-independent and also applies under a combined high temperature–high strain rate.

$$\sigma_{Eq}(\epsilon, T, \dot{\epsilon}) = \sigma_{True}(\epsilon, T, \dot{\epsilon}) \cdot MLR(\epsilon - \epsilon_N) \tag{9}$$

The true curves of Figure 14, processed by Equations (8) and (9), delivered the function  $S(\epsilon, T)$ , which approximates the coupled effect of  $T$  and  $\epsilon$  on the steel MS1700, according to Figure 15.

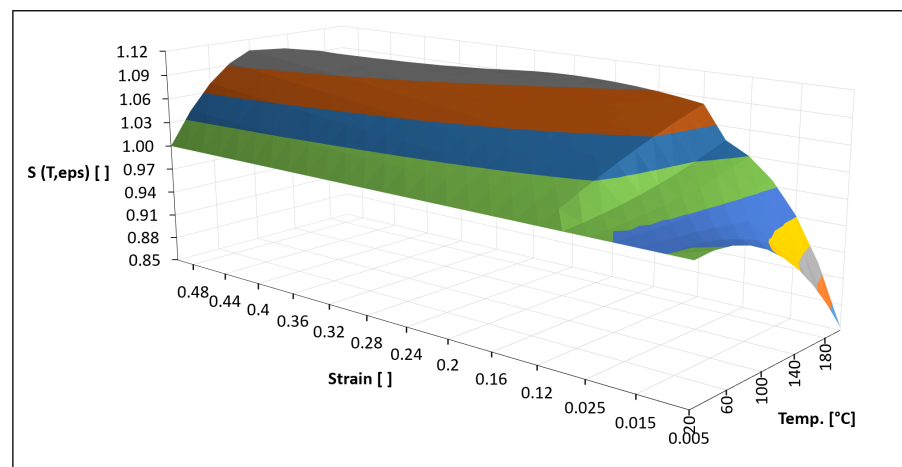


Figure 15. Thermal softening/hardening for the steel MS1700.

The transition in the thermal effect of the MS1700 is clearly visible in Figure 15 around necking onset ( $\epsilon_N \approx 0.03$ ): at early plastic stages (between first yield and necking onset), higher temperatures induce a thermal softening ( $S(\epsilon, T) < 1$ ); instead, in the postnecking plastic range, higher temperatures induce a thermal hardening ( $S(\epsilon, T) > 1$ ).

According to the knowledge of the authors, such non-monotonically varying dependence of the hardening on the temperature for different strain ranges is a rather uncommon feature.

Figure 15 also shows that  $\epsilon, T$  are strongly coupled to each other at early plastic stages; instead, beyond necking onset, the thermal response becomes rather insensitive to the strain and nearly depends on the temperature alone.

Metals subjected to temperature increase typically exhibit decreasing flow stress and lower stress–strain curves (thermal softening), although the opposite response of “negative softening”, proved in Figure 14b for the MS1700 steel, is also reported in the literature for other alloys [31–35].

5.2. Dynamic Tests at (Initial) Room Temperature

Figure 16 reports the true curves from the dynamic tests on the DP1000 and the MS1700 steels, while Table 4 reports the strains at the onset of diffused necking ( $\epsilon_{Neck}$ ) and localized necking ( $\epsilon_{Loc-Neck}$ ) calculated from the slopes of the stress–strain curves (respectively, according to the conditions  $\frac{\partial\sigma}{\partial\epsilon} = \sigma$  and  $\frac{\partial\sigma}{\partial\epsilon} = \sigma/2$ ), together with the failure strains according to the corrected-area and the DIC peak approaches.

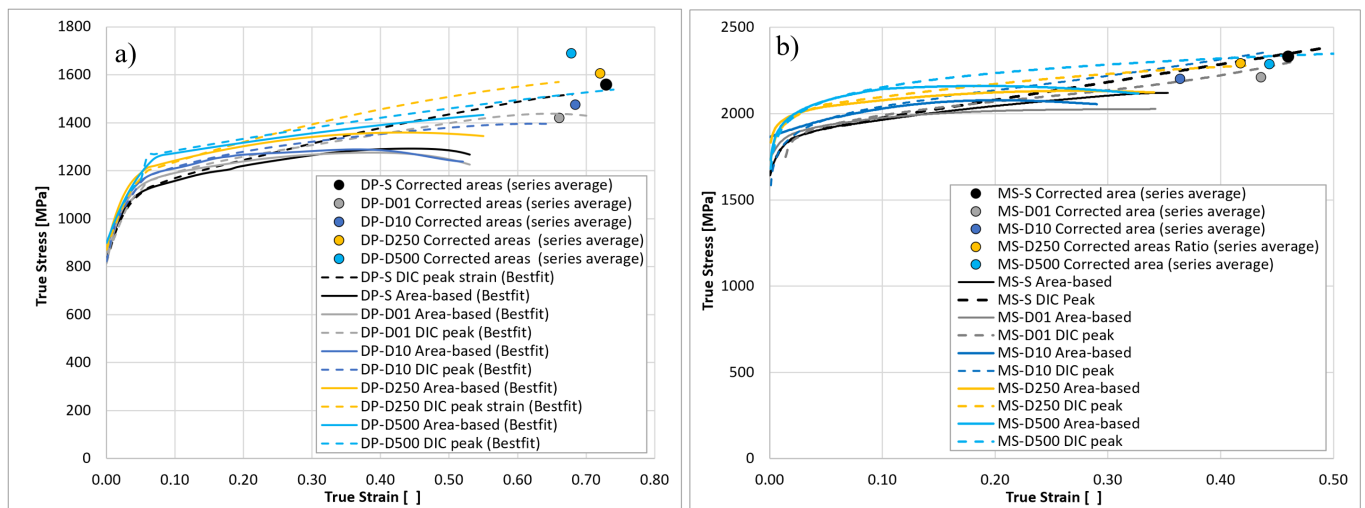


Figure 16. True curves from dynamic tests of the DP (a) and MS (b) materials.

Table 4. Strains at necking onset and failure according to the area-based and DIC peak procedures.

Test Series	$\epsilon_{Neck}$ (Avg Area-Based and DIC Peak)	$\epsilon_{Loc-Neck}$ (Avg Area-Based and DIC Peak)	$\epsilon_{Failure}$ (Corrected Area)	$\epsilon_{Failure}$ (DIC Peak)
DP-S-T20	0.07	0.14	0.73	0.71
DP-S-T100	0.05	0.20	0.63	0.57
DP-S-T200	0.07	0.19	0.41	0.31
DP-D01	0.07	0.13	0.66	0.70
DP-D10	0.07	0.12	0.68	0.65
DP-D250	0.09	0.12	0.72	0.75
DP-D500	0.08	0.11	0.69	0.53
MS-S-T20	0.03	0.09	0.46	0.55
MS-S-T100	0.03	0.14	0.40	0.47
MS-S-T200	0.04	0.15	0.32	0.34
MS-D01	0.02	0.07	0.44	0.51
MS-D10	0.02	0.10	0.36	0.51
MS-D250	0.03	0.06	0.55	0.48
MS-D500	0.04	0.09	0.44	0.57

The area-based true curves and the DIC peak curves in Figure 16 are coincident to each other until  $\varepsilon \approx 0.15$  for the DP1000 steel and  $\varepsilon \approx 0.1$  for the MS1700 steel, roughly corresponding to the onset of the localized necking.

Up to such strain values, the experimental stress–strain curves of each material exhibit an ascending–descending order, fully complying with the increasing–decreasing order of the imposed strain rates, proving a detectable sensitivity of both materials to the strain rate. At greater strains, the dynamic true curves reduce their slope, and before failure, the slower dynamic curves (those at 1/s and 10/s) even decrease below the static curves.

These trends indicate that at the first stages of dynamic test, where no remarkable temperature increase is yet developed, the dynamic amplification due to the strain rate is not opposed by any thermal softening and is clearly visible in Figure 16; instead, at later test stages, the increasing temperature causes a thermal softening to decrease the flow stress, which progressively balances and finally overcomes the dynamic amplification.

The outcome that thermal effects at dynamic rates consist of thermal softening is a substantial difference with respect to the thermal effect at static rates, which instead was found to be negligible for the DP1000 steel and to increase the flow stress for the MS1700 steel.

Further tests, at dynamic rates and initial temperatures  $T_0 > T_{Room}$ , should be performed for deriving such a coupled effect of  $\dot{\varepsilon}$  and  $T$  responsible for the change of thermal response from static to dynamic rates. However, this aspect exceeds the scopes of the present work, where the just dynamic amplification unaffected by any temperature effect is only derived from the early stages of dynamic tests.

The dynamic amplification, defined as the ratio of dynamic stress to static stress at a given strain,  $R = \sigma_{Dyn}(\varepsilon, \dot{\varepsilon}, T_{Room}) / \sigma_{Stat}(\varepsilon, T_{Room})$ , is reported in Figure 17 versus the current strain, for the tests MS-D01 and MS-D500.

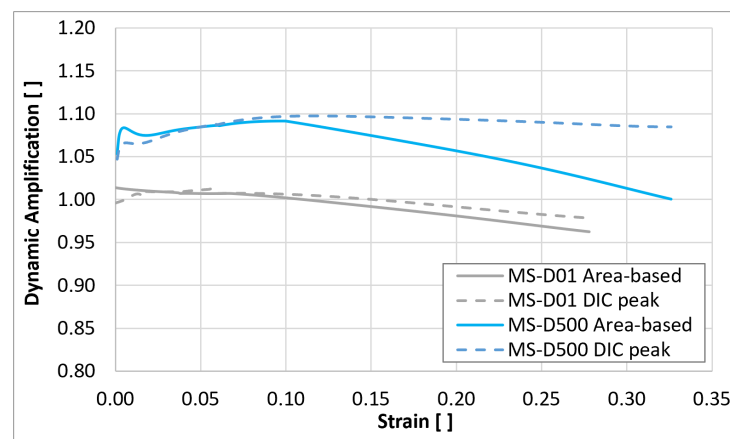


**Figure 17.** Dynamic amplification histories of tests MS-D01 and MD-D500.

Figure 17 shows that within  $\varepsilon \leq 0.1$ , the dynamic amplification is rather constant (just above 1% for the D01 tests and around 8% for the D500 tests); instead, beyond  $\varepsilon \approx 0.1$ , as expected, the localized necking causes rapidly increasing local temperatures and the aforementioned thermal effects, so that the plots in Figure 17 cease to express an almost “undisturbed” dynamic amplification and start expressing a mixed effect of rate and temperature.

Such trends are also qualitatively representative of the DP100 steel response for  $\varepsilon \leq 0.15$ ; therefore, the overall assessment of the strain rate effect for both metals is made in Figure 18 by collecting the values of the dynamic amplification at three discrete reference strains prior to the onset of localized necking and by plotting such values versus the current strain rate of each test.

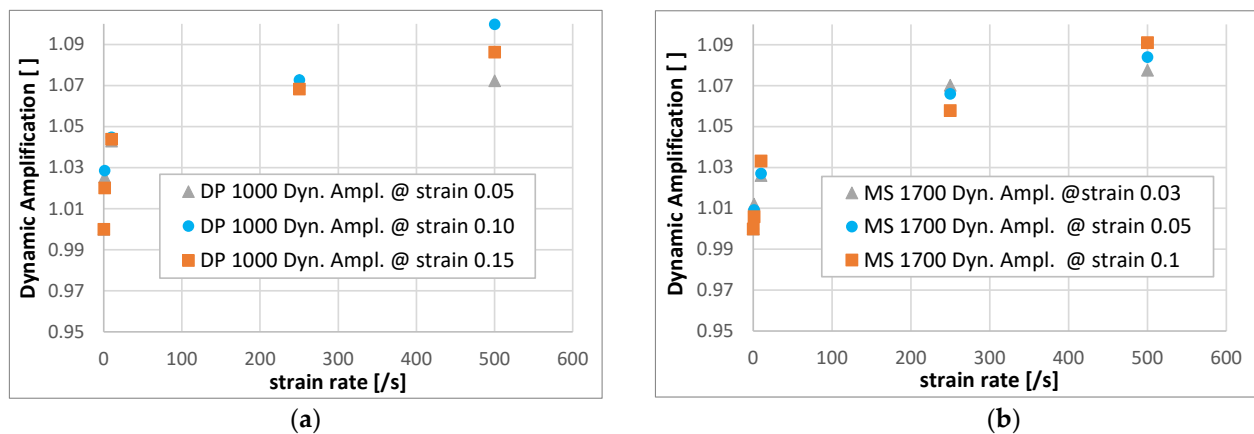


**Figure 18.** Dynamic amplification of DP1000 (a) and MS1700 (b) steels.

The dynamic amplifications of both metals are quite similar to each other, although that of the DP1000 steel is slightly higher (between 1 and 2%) than that of the MS1700 steel. Both steels exhibit a progressively increasing dynamic amplification spanning from 1–2% at lower rates investigated and up to 8–9% at 500/s.

The scattering of the failure strains for the MS1700 steel in Figure 16 is quite larger than that of the DP1000 steel, which is mainly because of the remarkably different accuracy in the waterjet cutting of the respective specimens series. Figure 19 shows the details of two representative undeformed specimens of the DP1000 (a) and MS1700 (b) steels with DIC speckles: the former specimen does not exhibit imperfections detectable by the naked eye at the scale of the picture; instead, the latter shows a remarkably undulated lower edge encircled by the yellow line.

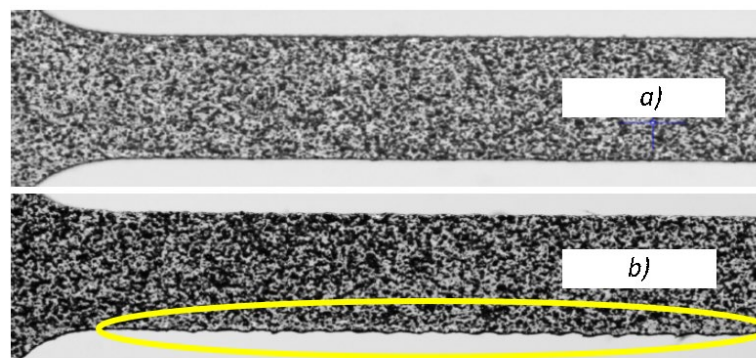


**Figure 19.** Specimen profile imperfections in the DP1000 (a) and the MS1700 (b) steels due to waterjet cutting.

While the geometrical imperfections of the MT1700 specimens cannot affect the plastic response up to  $\epsilon \approx 0.2$  (where large specimen volumes are interested by the macroscopic straining process), they are very likely capable of generating the experimental scattering of the MT1700 tests at the final stages, where stress and strain evolutions are limited to the very small specimen volumes of localized necking, and they are definitely sensitive to the shape of the specimen contour at the local scale.

The failure strains of the steel MS1700 clearly depend on the calculation procedure but are insensitive to the strain rate; in fact, they are very close to each other except for the D10 tests, where the early failure of a specimen (likely due to some manufacturing imperfection) lowered the average value of that triple specimens series.

The strain rate histories of D1 and D10 tests are plotted together in Figure 20a,b for the two steels respectively, with primary and secondary vertical axes scaled to each other

according to the same ratio 10:1 of the corresponding nominal rates. Similar considerations apply to the D250 and D500 tests, plotted in Figure 20c,d for the two steels respectively, where the scaling ratio of primary and secondary vertical axes is 2:1.

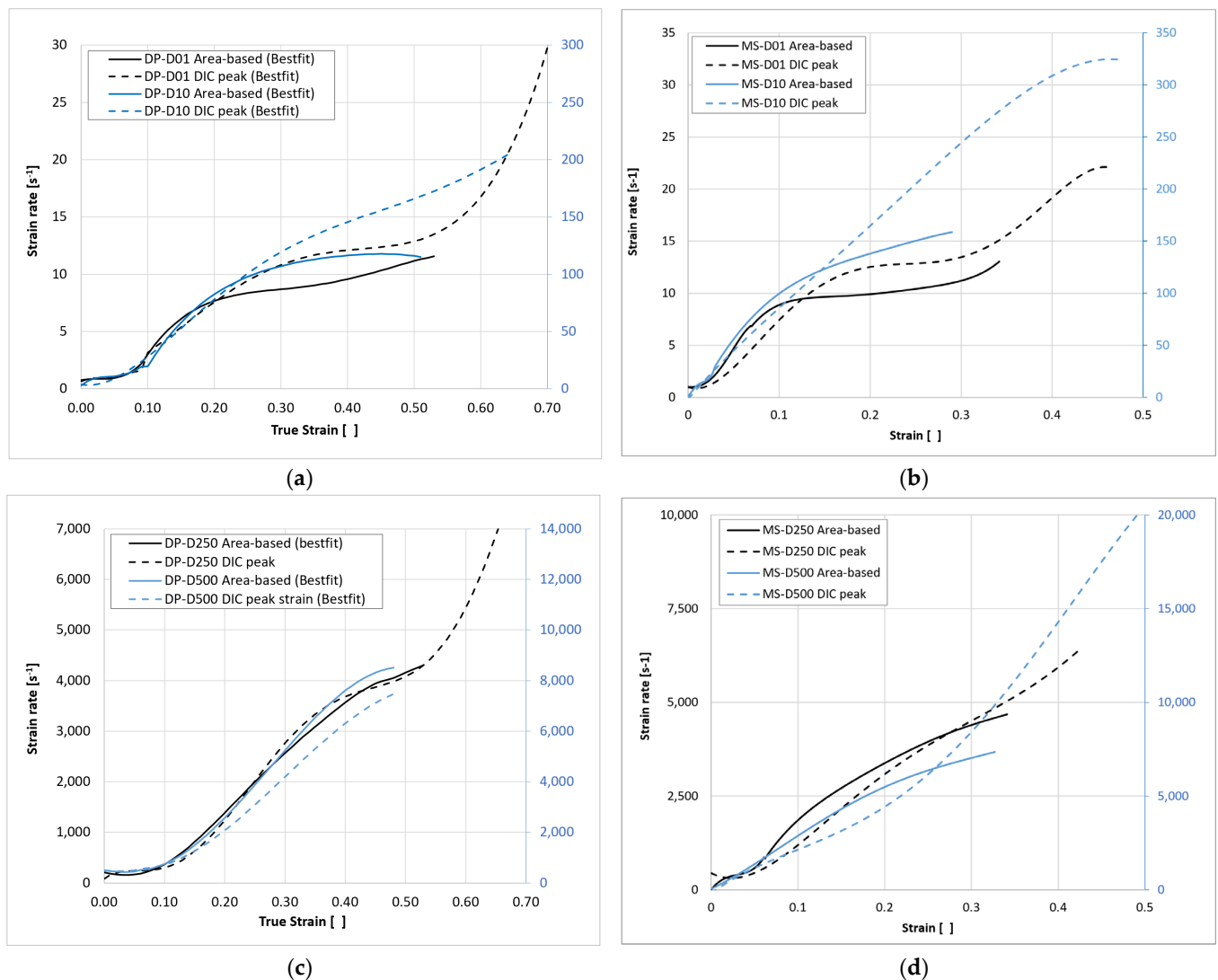


**Figure 20.** Strain rate histories of dynamic tests at intermediate ((a) DP, (b) MS) and high strain rates ((c) DP, (d) MS).

Each graph shows that, thanks to the above scaling of the vertical axes, the trends of the strain rate histories are similar to each other up to strain levels largely exceeding the onset of localized necking, where the true curves of each series started to scatter to each other. All the strain rate histories exhibit the initial short plateau before diffused necking onset (longer for the DP1000 with  $\varepsilon_N \approx 0.07$ , almost undetectable for the MS1700 with  $\varepsilon_N \approx 0.03$ ) and the successive burst of strain rate leading to magnifications of the strain rate up to a factor of 10 for the DP1000 steel and to a factor between 10 and 15 for the MT1700 steel. This trend is quite repeatable for both area-based and DIC peak approaches and fully supports the findings of previous works regarding different metals [12,13,16,17], confirming the generality of the observed phenomena.

At larger strains exceeding the onset of localized necking ( $\varepsilon > 0.4$  for the DP1000,  $\varepsilon > 0.2$  for the MS1700), bifurcations also develop between the strain rate histories derived by either the area-based or the DIC peak procedures, reflecting the progressive scattering increase attributed to very local variabilities intrinsic in the localized necking phenomena at approaching fracture, as already discussed for the true stress–true strain curves.

Recalling that dynamic tests also involve self-heating and that the hardening of the MS1700 steel is sensitive to the temperature, the question arises of whether or not any thermal effect should also be expected to show up in the true curves from dynamic tests of the MS1700 steel. Therefore, the temperature increase at the specimens' neck is estimated by assuming fully adiabatic straining (slightly approximate for the D01 tests but appropriate for faster dynamic tests) and full conversion of plastic work into heat (unit value of the Taylor–Quinney coefficient). The von Mises stress obtained by the MLR necking correction of Equation (9) is used to integrate the plastic work, and the resulting temperature histories up to  $\varepsilon = 0.2$  are plotted in Figure 21.

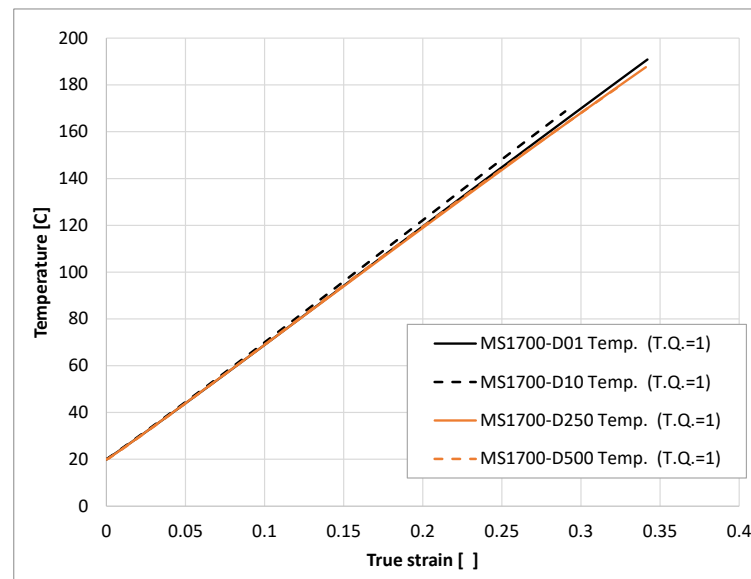


**Figure 21.** Temperature estimate from self-heating in dynamic tests.

The dynamic stress–strain curves of the steel MS1700, very close to each other, obviously delivered nearly identical temperature histories.

Within the necking onset ( $\varepsilon_n \approx 0.03$ ), no remarkable temperature increase has yet developed, which justifies that the dynamic stress–strain curves are unaffected by any thermal effect.

As strains close to 0.15 (quite beyond the onset of localized necking), the temperature becomes close to 100 °C; therefore, “negative” thermal softening (or thermally induced increase in the flow stress) around 5% should be expected, according to the temperature effect  $S(\varepsilon, T)$  derived from static tests. Instead, the dynamic stress–strain curves of MS1700 at such strain levels are still fully overlapped to the static ones.

This evidence suggests that the thermal function reported in Figure 15, derived at static rates, does not apply at dynamic rates and requires to be integrated by another function of the temperature, to be triggered at dynamic rates and likely expressing the coupled effect of  $\varepsilon, \dot{\varepsilon}, T$ .

This outcome is consistent to similar findings obtained in a previous work of the authors about A2-70 stainless steels [15]; however, further tests should be performed at dynamic rates and high temperatures with the materials at hand to separately assess the thermal effects at dynamic rates, which goes beyond the scope of the present work.

## 6. Conclusions

The characterization of DP1000 and MS1700 steel sheets for automotive applications is performed here at low–high strain rates and low–moderately high temperatures.

A preliminary assessment is made of experimental and postprocessing procedures for determining various estimates of stresses, strains and strain rates.

The true stress–true strain data based on the specimen elongation are confirmed to quit very soon being representative of the material response, especially for metals such as those at hand exhibiting early necking onset and more than 90% of their plastic life undergoing diffuse and localized necking.

The derivation of  $\sigma_{True}$ ,  $\varepsilon_{True}$  and  $\dot{\varepsilon}_{True}$  by optical measurements of the width of the shrinking specimen (area-based procedure) and by DIC strain readings at the midpoint of the width of the specimen neck (DIC peak procedure) delivered reliable predictions agreeing to each other up to nearly half of the material straining life, thus applying over strain intervals extended by a factor of 3 or 4 with respect to the strain intervals of the elongation-based true curves.

In the final half of the specimens' life, the increasing effect of the localized necking causes the area-based true curve to progressively underestimate the effective true stress; the DIC peak true curve remains a better approximation of such effective true curve, although some underestimation or overestimation can still occur, depending on the magnitude of the strain gradients through the thickness of the specimen.

Then, taking into account the distorted cross-section due to the localized necking improves the area-based estimate and at the same time is less sensitive to the scattering intrinsic in the local nature of DIC readings.

The static flow curves of both steels at different temperatures, obtained through the MLR postnecking correction of the true curves, allowed us to derive the function  $S(\varepsilon, T)$  expressing the coupled effect of temperature and strain at static rates, according to a general multiplicative hardening scheme. Such a temperature effect turned out to be negligible for the DP1000 steel; instead, for the MS1700 steel, it consisted of a thermal softening ( $S < 1$ ) at very early plastic stages before necking strain (close to 0.03), rapidly changing into a “negative thermal softening” or a “thermal hardening” ( $S > 1$ ) at strains around the necking onset and further increasing up to failure: the temperature of 200 °C increased the postnecking flow stress up to 9% with respect to the flow curve at room temperature.

The ratio of dynamic to static stress–strain curves allowed us to assess the strain rate sensitivity of the two sheet metals, although only the phases of each test extending up to nearly three times the necking strain have been considered, in order to avoid that also thermal effects due to the self-heating at dynamic rates and local variabilities due to the localized necking were included in such a ratio.

Both steels exhibited similar strain rate sensitivities, with dynamic amplifications progressively increasing from nearly 1% at strain rates of 1/s up to values around 9% at a strain of 500/s.

For the MS1700 steel, the strain rate of 500/s and the temperature of 200 °C generated comparable increases with respect to the static flow stress at room temperature, although the former mainly applied to early test phases, and the latter mainly applied to the postnecking strain range.

In addition, the strain rate histories from dynamic tests were evaluated according the area-based and the DIC peak procedures, delivering trends identical to each other up to large strains exceeding the onset of localized necking, then progressively bifurcating in the second half of the strain range for each test series. Both calculations procedures confirmed the spontaneous burst of strain rate occurring after necking onset, which was undetectable by the elongation-based approach typical of the technical regulations. Such a strain rate burst led to effective strain rates up to ten times greater than the nominal strain rates, as already pointed out by the authors in previous works.

**Author Contributions:** Conceptualization, G.M., M.M.T., D.D.C. and M.F.; Data curation, R.B.; Funding acquisition, G.M., M.M.T., D.D.C. and M.F.; Investigation, G.M. and R.B.; Methodology, G.M., R.B. and D.D.C.; Resources, M.M.T., D.D.C. and M.F.; Supervision, M.M.T., D.D.C. and M.F.; Visualization, R.B.; Writing—original draft, R.B.; Writing—review and editing, G.M. All authors have read and agreed to the published version of the manuscript.

**Funding:** This work was supported by the funding program “Ricerca di Ateneo 2020-22—Pia.Ce.Ri Linea 2—Project TMESPEMES” of the University of Catania—Italy.

**Data Availability Statement:** Not applicable.

**Conflicts of Interest:** The authors declare no conflict of interest.

## References

1. Cortis, G.; Nalli, F.; Sasso, M.; Cortese, L.; Mancini, E. Effects of Temperature and Strain Rate on the Ductility of an API X65 Grade Steel. *Appl. Sci.* **2022**, *12*, 2444. [[CrossRef](#)]
2. Joun, M.; Eom, J.G.; Lee, M.C. A New Method for Acquiring True Stress–Strain Curves over a Large Range of Strains Using a Tensile Test and Finite Element Method. *Mech. Mater.* **2008**, *40*, 586–593. [[CrossRef](#)]
3. Lattanzi, A.; Barlat, F.; Pierron, F.; Marek, A.; Rossi, M. Inverse Identification Strategies for the Characterization of Transformation-Based Anisotropic Plasticity Models with the Non-Linear VFM. *Int. J. Mech. Sci.* **2020**, *173*, 105422. [[CrossRef](#)]
4. Rossi, M.; Lattanzi, A.; Barlat, F. A General Linear Method to Evaluate the Hardening Behaviour of Metals at Large Strain with Full-Field Measurements. *Strain* **2018**, *54*, e12265. [[CrossRef](#)]
5. Bridgman, P.W. *Studies in Large Plastic Flow and Fracture: With Special Emphasis on the Effects of Hydrostatic Pressure*; Harvard University Press: Cambridge, MA, USA, 2013. [[CrossRef](#)]
6. Mirone, G. Approximate Model of the Necking Behaviour and Application to the Void Growth Prediction. *Int. J. Damage Mech.* **2004**, *13*, 241–261. [[CrossRef](#)]
7. Peirs, J.; Verleysen, P.; Van Paeppegem, W.; Degrieck, J. Determining the Stress–Strain Behaviour at Large Strains from High Strain Rate Tensile and Shear Experiments. *Int. J. Impact Eng.* **2011**, *38*, 406–415. [[CrossRef](#)]
8. Abedini, A.; Narayanan, A.; Butcher, C. An Investigation into the Characterization of the Hardening Response of Sheet Metals Using Tensile and Shear Tests with Surface Strain Measurement. *Forces Mech.* **2022**, *7*, 100090. [[CrossRef](#)]
9. Mirone, G.; Verleysen, P.; Barbagallo, R. Tensile Testing of Metals: Relationship between Macroscopic Engineering Data and Hardening Variables at the Semi-Local Scale. *Int. J. Mech. Sci.* **2019**, *150*, 154–167. [[CrossRef](#)]
10. Mirone, G.; Corallo, D.; Barbagallo, R. Interaction of Strain Rate and Necking on the Stress-Strain Response of Uniaxial Tension Tests by Hopkinson Bar. *Procedia Struct. Integr.* **2016**, *2*, 974–985. [[CrossRef](#)]
11. Mirone, G.; Barbagallo, R.; Corallo, D.; Di Bella, S. Static and Dynamic Response of Titanium Alloy Produced by Electron Beam Melting. *Procedia Struct. Integr.* **2016**, *2*, 2355–2366. [[CrossRef](#)]
12. Mirone, G.; Barbagallo, R.; Giudice, F. Locking of the Strain Rate Effect in Hopkinson Bar Testing of a Mild Steel. *Int. J. Impact Eng.* **2019**, *130*, 97–112. [[CrossRef](#)]
13. Mirone, G.; Corallo, D.; Barbagallo, R. Experimental Issues in Tensile Hopkinson Bar Testing and a Model of Dynamic Hardening. *Int. J. Impact Eng.* **2017**, *103*, 180–194. [[CrossRef](#)]
14. Mirone, G.; Barbagallo, R.; Giudice, F.; Di Bella, S. Analysis and Modelling of Tensile and Torsional Behaviour at Different Strain Rates of Ti6Al4V Alloy Additive Manufactured by Electron Beam Melting (EBM). *Mater. Sci. Eng. A* **2020**, *793*, 139916. [[CrossRef](#)]
15. Mirone, G.; Barbagallo, R. How Sensitivity of Metals to Strain, Strain Rate and Temperature Affects Necking Onset and Hardening in Dynamic Tests. *Int. J. Mech. Sci.* **2021**, *195*, 106249. [[CrossRef](#)]
16. Mirone, G. The Dynamic Effect of Necking in Hopkinson Bar Tension Tests. *Mech. Mater.* **2013**, *58*, 84–96. [[CrossRef](#)]
17. Zhang, L.; Pellegrino, A.; Petrinic, N. Dynamic Necking of a near  $\alpha$  Titanium Alloy at High Strain Rates: Experiments and Modelling. *Def. Technol.* **2021**, *17*, 1126–1134. [[CrossRef](#)]
18. Zhang, L.; Pellegrino, A.; Townsend, D.; Petrinic, N. Strain Rate and Temperature Dependent Strain Localization of a near  $\alpha$  Titanium Alloy. *Int. J. Impact Eng.* **2020**, *145*, 103676. [[CrossRef](#)]
19. Jacques, N.; Rodríguez-Martínez, J.A. Influence on Strain-Rate History Effects on the Development of Necking Instabilities under Dynamic Loading Conditions. *Int. J. Solids Struct.* **2021**, *230–231*, 111152. [[CrossRef](#)]
20. Chandran, S.; Liu, W.; Lian, J.; Münstermann, S.; Verleysen, P. Strain Rate Dependent Plasticity and Fracture of DP1000 Steel under Proportional and Non-Proportional Loading. *Eur. J. Mech. A Solids* **2022**, *92*, 104446. [[CrossRef](#)]
21. Hui, L.; Rui, F. Dynamic Deformation Behavior and Corresponding Constitutive Model of Ultra-High Strength DP1000 Steel. *J. Constr. Steel Res.* **2022**, *191*, 107188. [[CrossRef](#)]
22. Cadoni, E.; Singh, N.K.; Forni, D.; Singha, M.K.; Gupta, N.K. Strain Rate Effects on the Mechanical Behavior of Two Dual Phase Steels in Tension. *Eur. Phys. J. Spec. Top.* **2016**, *225*, 409–421. [[CrossRef](#)]
23. Liu, W.; Lian, J.; Münstermann, S. Damage Mechanism Analysis of a High-Strength Dual-Phase Steel Sheet with Optimized Fracture Samples for Various Stress States and Loading Rates. *Eng. Fail. Anal.* **2019**, *106*, 104138. [[CrossRef](#)]

24. Xia, P.; Vercruyssen, F.; Petrov, R.; Sabirov, I.; Castillo-Rodríguez, M.; Verleysen, P. High Strain Rate Tensile Behavior of a Quenching and Partitioning (Q&P) Fe-0.25C-1.5Si-3.0Mn Steel. *Mater. Sci. Eng. A* **2019**, *745*, 53–62. [[CrossRef](#)]
25. Ruggiero, A.; Bonora, N.; Gentile, D.; Iannitti, G.; Testa, G.; Colliander, M.H.; Masaggia, S.; Vettore, F. Strain Rate Effects on Fracture Behavior of Austempered Ductile Irons. *AIP Conf. Proc.* **2018**, *1979*, 70028.
26. Scapin, M.; Peroni, L.; Fichera, C. Investigation of Dynamic Behaviour of Copper at High Temperature. *Mater. High Temp.* **2014**, *31*, 131–140. [[CrossRef](#)]
27. Kabirian, F.; Khan, A.S.; Gnäupel-Herlod, T. Plastic Deformation Behavior of a Thermo-Mechanically Processed AZ31 Magnesium Alloy under a Wide Range of Temperature and Strain Rate. *J. Alloy. Compd.* **2016**, *673*, 327–335. [[CrossRef](#)]
28. Jia, B.; Rusinek, A.; Pesci, R.; Bahi, S.; Bernier, R. Thermo-Viscoplastic Behavior of 304 Austenitic Stainless Steel at Various Strain Rates and Temperatures: Testing, Modeling and Validation. *Int. J. Mech. Sci.* **2020**, *170*, 105356. [[CrossRef](#)]
29. Wen, D.; Wang, J.; Wang, K.; Xiong, Y.; Huang, L.; Zheng, Z.; Li, J. Hot Tensile Deformation and Fracture Behaviors of a Typical Ultrahigh Strength Steel. *Vacuum* **2019**, *169*, 108863. [[CrossRef](#)]
30. Alharbi, K.; Ghadbeigi, H.; Efthymiadis, P.; Zanganeh, M.; Celotto, S.; Dashwood, R.; Pinna, C. Damage in Dual Phase Steel DP1000 Investigated Using Digital Image Correlation and Microstructure Simulation. *Model. Simul. Mater. Sci. Eng.* **2015**, *23*, 85005. [[CrossRef](#)]
31. Xiao, H.; Baker, I. The temperature dependence of the flow and fracture of Fe-40A. *Scr. Metall. Et Mater.* **1993**, *28*, 1411–1416. [[CrossRef](#)]
32. Caillard, D.; Couret, A. Dislocation Cores and Yield Stress Anomalies. In *Dislocations in Solids*; Elsevier: Amsterdam, The Netherlands, 1996; Volume 10, pp. 69–134. ISBN 978-0-444-82370-0.
33. Guo, J.T.; Jin, O.; Yin, W.M.; Wang, T.M. Discovery and study of anomalous yield strength peak in FeAl alloy. *Scr. Metall. Et Mater.* **1993**, *29*, 783–785. [[CrossRef](#)]
34. Liu, W.; Lian, J. Stress-State Dependence of Dynamic Strain Aging: Thermal Hardening and Blue Brittleness. *Int. J. Miner. Metall. Mater.* **2021**, *28*, 854–866. [[CrossRef](#)]
35. Wu, D.; Baker, I.; Munroe, P.R.; George, E.P. The Yield Strength Anomaly of Single-Slip-Oriented Fe–Al Single Crystals. *Intermetallics* **2007**, *15*, 103–107. [[CrossRef](#)]